

Large eddy simulation of serration effects on an ultra-high bypass-ratio engine exhaust jet

Zhong-Nan Wang, James Tyacke and Paul Tucker

Department of Engineering, University of Cambridge, Cambridge CB2 1PZ, UK

Abstract

Serrated jet nozzles are considered to be an efficient and practical passive control approach for jet noise. However, some fundamental mechanisms of serration effects on jet noise are not fully understood, especially in terms of the sound source. In this paper, a high fidelity simulation framework using large-eddy simulation (LES) is demonstrated to predict near-field turbulence and far-field acoustics from an ultra-high-bypass-ratio engine with round and serrated nozzles. Far-field sound is predicted using Ffowcs Williams-Hawkings (FWH) integration. The results show that the serrated nozzle increases mixing near the nozzle and hence the turbulence decay rate, reducing the turbulence level downstream. The serrations shift the energy from the low frequencies to the high frequencies and decrease overall sound pressure levels by about 3dB over low frequency range. Sound sources are analyzed based on 4th order space-time correlations. There are six major source components (R_{1111} , R_{2222} , R_{3333} , R_{1313} , R_{1212} and R_{2323}) inside jet shear layers. The serrations are able to reduce the amplitude of these source terms, causing them to decay rapidly to a level below the round nozzle jet within $2D$ downstream of the nozzle.

Keywords: Large-eddy simulation, Ultra-high bypass-ratio (UHBPR) engine, Noise reduction, Serrated nozzle

1. Introduction

Aircraft noise has become a major concern to residents neighbouring airports when the air traffic volume is increasing dramatically nowadays. Among aircraft

noise sources, jet noise is the dominant component when an aircraft takes off.
5 Research about the jet noise dates back to Lighthill and his celebrated 8th power
law [1]. Since then, considerable progress has been made in this field but the
main noise reduction technology still follows the guidance of lighthill theory
and relies mainly on reducing the exhaust exit velocity by aeroengine bypass
ratio increase [2]. Some current research shows that noise reduction can be
10 achieved by altering the flow structures responsible for sound generation without
substantially reducing exhaust velocity [3] and it can be accomplished through
active and passive control [4]. Therefore, more insight into jet turbulence and
its effects on sound sources is needed to explore the potential of noise control
strategies.

15 Noise control strategies are considered if it is not practical to increase the
bypass ratio any further. For example, engines become so large in diameter that
there is little room between the engine and the ground or wing. Nozzle serrations
are regarded as an effective noise control technology without bypass ratio
increase and has been successfully used on several civil aeroengines. Research
20 into the effects of nozzle serrations on jet noise was first focused on isolated
jets [5, 6, 7]. It shows that the serrations can break down large coherent flow
structures and reduce the isolated jet noise at low polar angles. Mengle [8, 9]
tried to design azimuthally varying chevrons (serrations) to reduce installation
noise generated when the jet is mounted to the airframe and test them exper-
25 imentally. However, due to lack of detailed unsteady flow data, the serration
effects haven't been fully understood and the design of serrations mainly relies
on empirical experience gained from a range of limited rig tests.

Large-eddy simulation (LES) is a reliable method to capture the flow struc-
tures that are responsible for sound generation. Compared to experiments, it
30 can provide much more insight into the unsteady flow field and reveal the sound
source mechanisms. It has proved to be a reliable predictive tool for jet noise
[10] and has been successfully used to simulate single stream round [11, 12] and
serrated jets[13] and coaxial dual stream jets[14, 15]. In this paper, an LES
framework is demonstrated to simulate an ultra-high bypass-ratio (UHBPR) jet

35 engine with and without serrations. The paper explores serration effects on the
jet flow, acoustics and its sources using the LES data. It also show its potential
and mechanism to reduce jet noise in the circumstance of UHBPR aeroengines.
The article is organized into three parts: First, the simulated cases are intro-
duced. Then the simulation methodology is shown, describing LES methods and
40 a modular hybrid mesh strategy for serrated nozzles. Finally the LES results
are analysed from the perspectives of jet aerodynamics and acoustics.

2. Case description

The simulation is performed for an UHBPR jet. Two cases are numerically
simulated in this paper to investigate the serration effects. One is the baseline
45 round nozzle, the other is the serrated nozzle. Figure 1 shows the overlap of two
nozzle geometries. The serrations are shown in blue and the baseline nozzle in
pale yellow. 16 serrations are designed around the bypass nozzle edge to increase
near-nozzle mixing. The serration roots are set slightly backward compared to
the baseline nozzle lip, however the tips protrude further downstream. This
50 is to reduce the serration penalties on nozzle performance. The bypass and
core mass flow remain unaltered. The two nozzles are operating at the same
condition and under an outer flight stream of 90m/s. The nozzle operating
conditions are summarized by Table 1. The corresponding Reynolds and Mach
numbers based on bypass velocity and nozzle diameter are 3×10^6 and 0.66.
55 The bypass ratio of the nozzle is around 15, which is representative of UHBPR
engines. By comparing these two cases, the serration effects can be quantified.

Table 1: Jets operating condition

	p_0/p_a	T_0/T_a	$\dot{m}(kg/s)$
Bypass	1.342	1.128	6.373
Core	1.222	2.652	0.414

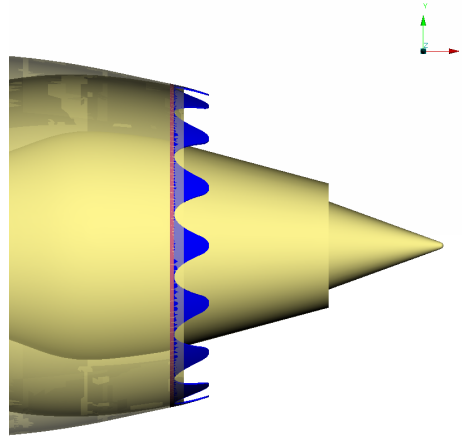


Figure 1: Overlay of baseline and serrated nozzle geometries

3. Methodology

To predict this flow, LES is used to simulate large turbulent structures in the jet plume and RANS to model streaks in the attached boundary layers on the nozzle. The methodology, including turbulence modelling, serrated nozzle
60 meshing strategy and far-field sound prediction, are introduced as follows.

3.1. Hybrid LES-RANS turbulence modelling

The solver used here is an edged-based finite volume code. The compressible flow equations are solved in the discretized integral form.

$$\Omega_i \frac{\partial U_i}{\partial t} = \sum_{j \in E(i)} (F_{ij}^{v,n} - F_{ij}^{c,n}) S_{ij}^n \quad (1)$$

65 where subscript i represents in the mesh element i and ij represents on the control surface between the mesh element i and j . The superscript n represents surface normal direction pointing outwards the control volume. $E(i)$ is the set of elements neighboring the the element i . Ω is the volume of the mesh element. U represents the conservative variables $[\rho, \rho \vec{u}, \rho E]$, $F^{v,n}$ represents
70 surface-normal viscous fluxes $[0, \vec{\tau}^n, \vec{\tau}^n \cdot \vec{u} - q^n]$ and $F^{c,n}$ represents convective

fluxes $[\rho u^n, \rho \vec{u} u^n + p \vec{n}, \rho H u^n]$. ρ , u , E , H , τ and q are flow density, velocity, total internal energy, total enthalpy, viscous stress and heat conduction respectively.

In LES, around 90 percent of turbulence kinetic energy needs to be resolved and this requires non-dissipative high-resolution numerical schemes. In this
75 study, a non-dissipative numerical method is utilised to preserve kinetic energy [16] and has been shown to correctly predict the turbulence energy cascade [14, 17]. The numerical convective flux contains two parts and can be written as

$$F_{ij}^{c,n} = F_{ij,KEP}^n - \frac{1}{2} \varepsilon |A_{ij}^{c,n}| [L(U_j) - L(U_i)] \quad (2)$$

where, $F_{ij,KEP}^n$ is the kinetic energy preseving fluxes $[\overline{\rho u^n}, \overline{\rho \vec{u} u^n} + \overline{p \vec{n}}, \overline{\rho H u^n}]$,
80 the overbar is the arithmetic averaging operator using the values in the adjacent mesh elements i and j . $A_{ij}^{c,n}$ is the surface-normal Jacobian matrix $\frac{\partial F_{ij}^{c,n}}{\partial U}$, L is the Laplacian operator $\frac{\partial^2}{\partial x_k \partial x_k}$. The parameter ε controls artificial dissipation in the simulation.

The first part of this flux is non-dissipative kinetic energy preserving scheme
85 and has low sensitivity to grid cell types, allowing a range of mesh topologies to be utilised. It is designed to perform LES with low dissipation. The second part is numerical smoothing. This is used to provide the sponge region towards the computation domain boundary and stabilize the computation. The viscous fluxes $F_{ij}^{v,n}$ are calculated using central difference method. The time derivatives
90 $\frac{\partial U_i}{\partial t}$ are discretized by the 2^{nd} order backward Euler scheme and coupled with dual time stepping for unsteady simulations.

To avoid the severe cost of resolving near-wall streaks at the high Reynolds number considered ($Re = \frac{U_{flight} D_{bypass}}{\nu} = 2 \times 10^6$), RANS layer are used to model the boundary layers on the nozzle surfaces. The RANS layer is blended
95 with the LES region based on a modified wall distance [18]. The blending is achieved at the stress level, the Spalart-Allmaras (SA) RANS model stresses [19] are hybridized with non-linear SGS stresses [20]. The hybrid turbulence model stress is expressed as

$$\tau_{ij}^{model} = \bar{L} + \overline{NL} \quad (3)$$

where, \bar{L} and \overline{NL} represent the linear and non-linear part, respectively, of
 100 the modelled turbulence stress. The blended linear and nonlinear stress terms
 are

$$\bar{L} = \frac{\tau_{kk}\delta_{ij}}{3} + 2[f \cdot \mu_{SGS} + (1-f) \cdot \mu_{RANS}]S_{ij} \quad (4)$$

$$\overline{NL} = \rho C_\alpha \Delta^2 f \left(\frac{\partial u_i}{\partial x_l} \frac{\partial u_l}{\partial x_j} + \frac{\partial u_i}{\partial x_l} \frac{\partial u_j}{\partial x_l} + \frac{\partial u_l}{\partial x_i} \frac{\partial u_l}{\partial x_j} \right) \quad (5)$$

where, $S_{ij} = 0.5(\partial u_i/\partial x_j + \partial u_j/\partial x_i)$ is the strain rate tensor, $\Delta = vol^{1/3}$ is
 the filter length. The blending function f is based on the wall distance d , which
 becomes one in the LES region.

$$f(d) = \min\left[\max\left(\frac{d - (1-\beta)d_{RANS}}{\beta d_{RANS}}, 0\right), 1\right] \quad (6)$$

105 d_{RANS} represents the specified RANS layer thickness, and β defines the
 size of RANS-to-LES transition zone. The blending function is shown with the
 computed SA RANS variable in Fig 2.

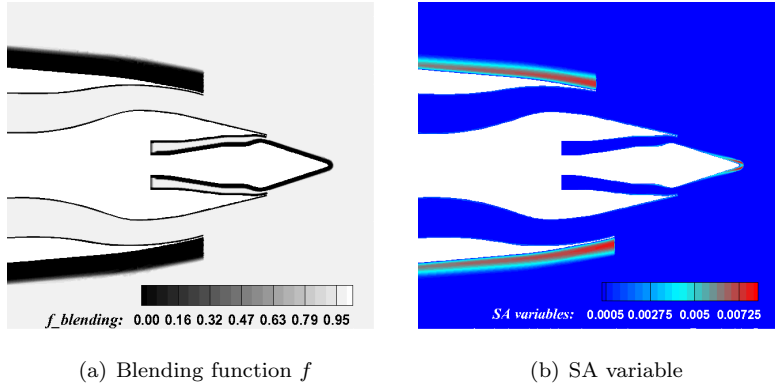


Figure 2: Interactions between the jet and the wing/flap

Far-field characteristic free-stream boundary conditions are set at the side
 and flight-inlet boundaries. Static pressure is set at the outlet boundary and to-

110 tal pressure and total temperature at the core and bypass duct inlet. To reduce
the numerical reflection, high-dissipative sponge regions are placed near the com-
putational boundaries. Turbulence is triggered naturally by Kelvin-Helmholtz
instability using turbulent boundary profile from RANS layer near the nozzle
wall and transition happens immediately within half diameter downstream the
115 nozzle. The simulation is collected for around $200 D_{bypass}/U_{bypass}$ for statistics
and spectra calculation. As estimated in [14], the cost of this type simulation
can be €13-18k for the current grid scale, while the typical jet noise rig testing
costs around €200k.

3.2. Serrated nozzle mesh strategy

120 Meshing the serrated bypass nozzle geometry is challenging due to its irreg-
ular nozzle shape. Serrations also generate azimuthally varying shear layers. To
follow the serration-generated shear layers, a modular mesh strategy is used,
implanting regions of unstructured mesh within the structured jet plume mesh.
Figure 3(a) shows the modular mesh topology for serration shear layers. The
125 numerics are less dissipative on hexahedral meshes and thus hexahedrons are
better for eddy resolving simulation [14]. The majority of the jet plume is
meshed with hexahedral elements while the serrations and the shear layer are
modelled using modular hybrid structured-unstructured meshes. This topology
allows high-quality mesh to be generated locally near serrations and most im-
130 portantly the azimuthal resolution can be adapted according to the smaller flow
scales near the nozzle introduced by the serrations. The modular mesh sections
are based on prism layers extruded from quad-dominant surface meshes. It pro-
duces a hexahedral dominant volume mesh. The mesh aligns with shear layer
variations in the azimuthal direction, shown in Fig 3(b).

135 Except for the modular section, the mesh used for the serrated nozzle is the
same as that for the baseline round nozzle. Table 2 shows the grid statistics.
There is around a 25% and 32 % increase in node and edge number for the ser-
rated nozzle mesh, which roughly corresponds to the simulation resolution and
cost. These increases are caused by the serration-introduced smaller azimuthal

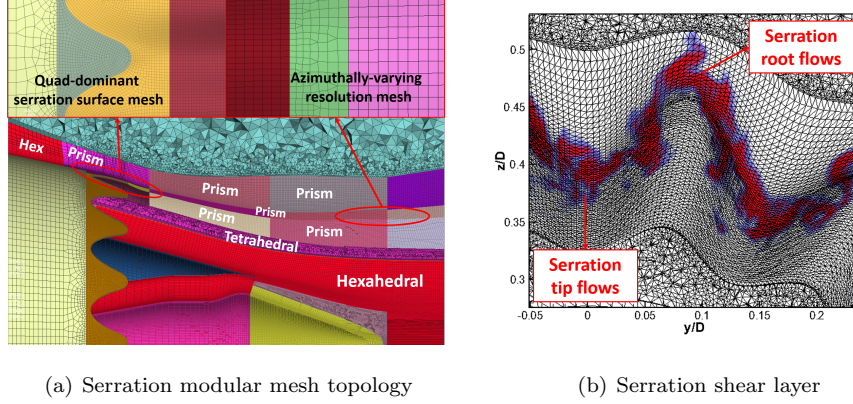


Figure 3: Serrated nozzle shear layer and its modular mesh

140 structures near the nozzle that have to be resolved.

Table 2: Mesh statistics for baseline and serration jets ($N \times 10^6$)

	N_{node}	$N_{hexahedron}$	$N_{tetrahedron}$	$N_{pyramid}$	N_{prism}	N_{cell}	N_{edge}
Baseline	32	29	16.8	0.22	0.032	46.2	107.6
Serration	40.2	34.7	30.5	0.57	0.38	66.2	141.7

3.3. Far-field sound prediction

Far field sound is predicted using the Ffowcs William-Hawkings (FW-H) equation from recorded flow time series on near field surfaces. These surfaces are placed in the irrotational region to avoid hydrodynamic contamination of the acoustic predictions. The approximate FW-H surface placement in the near field is shown in Fig 4. The convective formula [21] is used for sound prediction because the jets are operating under a forward flight stream. The formula can be written as

$$4\pi\tilde{p}'(\mathbf{x}, t) = \int_S \left[(1 - M_0\tilde{R}_1) \frac{\dot{Q}_i n_i}{R^*} - U_0 \frac{\tilde{R}_1^* Q_i n_i}{R^{*2}} \right] dS + \int_S \left[\frac{\dot{L}_{ij} n_j \tilde{R}_i}{c_0 R^*} + \frac{L_{ij} n_j \tilde{R}_i^*}{R^{*2}} \right] dS \quad (7)$$

where, \mathbf{x} is observer location and \mathbf{y} is source location. U_{0j} is the flight
150 stream velocity in the x_j -direction. The mass flux is $Q_i = \rho U_i - \rho_0 U_{0i}$, the
momentum flux is $L_{ij} = \rho u'_i(u'_j + U_{0j}) + p' \delta_{ij}$. The time derivative is expressed
by $\dot{(*)} = \partial(*)/\partial t$, while the spatial derivative is expressed by $(\tilde{*)}_i = \partial(*)/\partial x_i$.
The acoustic distance R^* , flight stream factor β and radiation distance R are
defined as

$$R^* = \sqrt{(x_1 - y_1)^2 + \beta[(x_2 - y_2)^2 + (x_3 - y_3)^2]} \quad (8)$$

$$\beta = \sqrt{1 - M_0^2} \quad (9)$$

$$R = \frac{-M_0(x_1 - y_1) + R^*}{\beta^2} \quad (10)$$

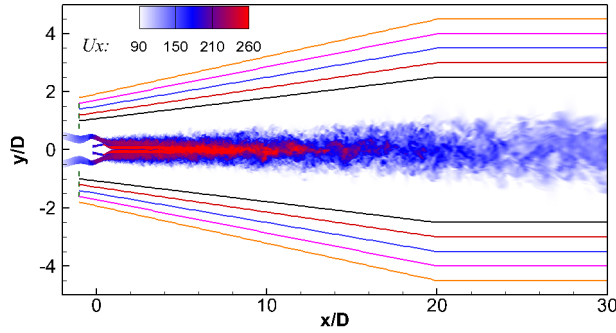


Figure 4: FW-H integral surfaces near-field placement

155 4. Results

Validation of the methodology can be found in [11, 12, 13, 14, 17] and sum-
marized in the appendix. In this section, the serration effects are discussed
using LES data from perspectives of flow and acoustics. The sound sources are
explored using 4th order space-time correlations.

160 4.1. Flow field

Figure 5 shows an overview of the LES results on flows and acoustics from
serration nozzle. The relatively small turbulent structures introduced by the ser-

rated nozzle are resolved by the current grid. The small hairpin vortex structures develop from the serration root and gradually grow into larger size downstream. This tends to increase turbulent mixing and also dissipates energy faster. The eddies are coloured by radial velocity component. The flow from the serration root has larger radial velocity than that from the serration tip because of serration penetration. Downstream of the nozzle serrations, the serration root flow is moving outwards while the serration tip flow is moving relatively inwards. This forms a pair of streamwise vortices downstream of each serration. Compared with round nozzle jets, the serrations break up the axi-symmetric azimuthal ring-like coherent structures into smaller scale roll-up structures. This has a calming effect of reducing the overall turbulence that is to be shown in the following paragraphs. This supports the hypothesis in [5] that the early break-up of the azimuthal structures near the nozzle helps to reduce the noise by decreasing the downstream turbulence level.

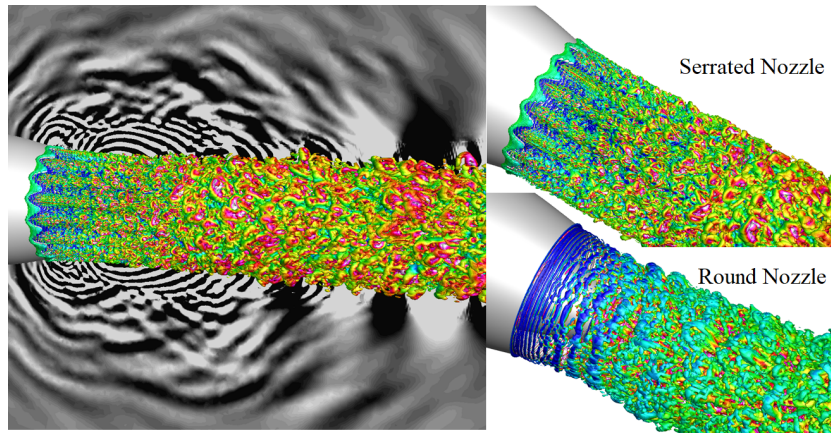
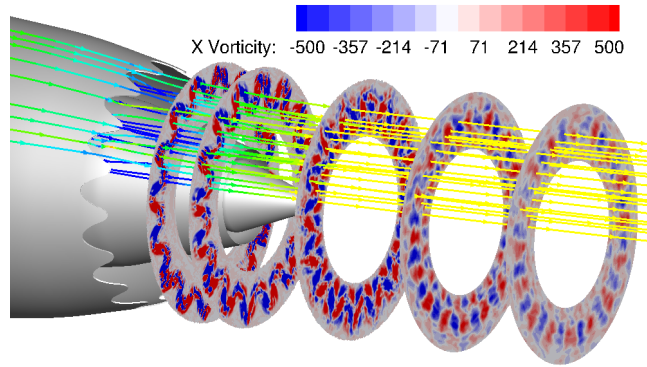


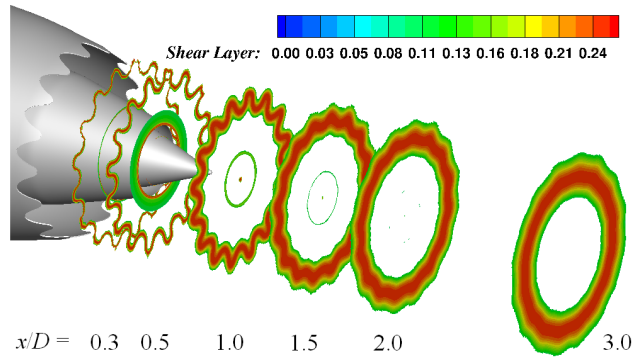
Figure 5: Q-criterion coloured by radial velocity with $\frac{dp}{dt}$ indicating the acoustic field

The serration-induced streamwise vortices break up the azimuthal coherent structures, they are better visualized in Fig. 6(a) using axial vorticity. The streamlines are also coloured by radial velocity. It shows that a pair of streamwise vortices are generated by each serration near the nozzle. They further induce secondary vortices downstream i.e. $x/D = 1$, which contribute to in-

creased mixing and dissipation. These streamwise vortices are also dissipated quickly when being convected downstream. This is a result of the relatively smaller size of civil aeroengine serrations than the more aggressive serrations studied previously [13]. Thus the streamwise vorticity increased mixing is confined in the near nozzle region. Another aspects of these streamwise vortices can be seen as azimuthal variation of shear layer, it is shown in Fig. 6(b).



(a) Streamwise vortices



(b) Serrated nozzle shear layer

Figure 6: Streamwise vortices and shear layer development for the serrated nozzle

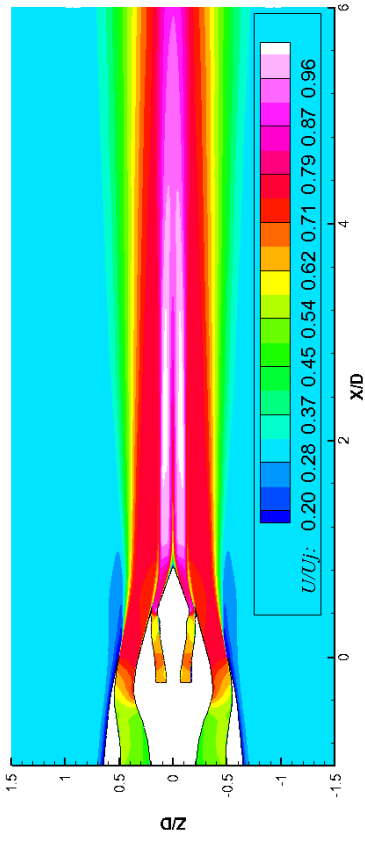
For the time-mean flow field, Fig. 7 shows a direct comparison between the baseline and serration jets. The jets are under the influence of a flight stream, so the spreading is reduced radially. However, serration effects on flow velocity

are still evident near the nozzle. The jet spreads rapidly at the serration roots and contracts at the tips. This causes the shear layer to vary periodically in the azimuthal direction and characterizes the initial development of serrated nozzle jets. As noted previously, the shear layer trajectory from the serrated nozzle is varied in the azimuthal direction (see Fig. 6(b)).

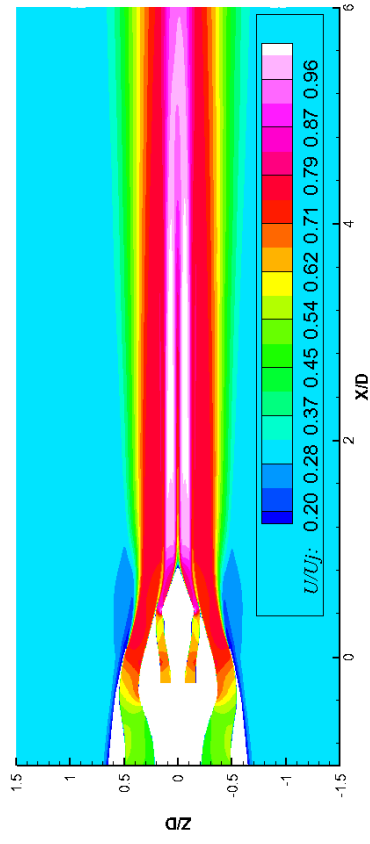
As for turbulent fluctuations in Fig. 8, serrations shrink the high turbulence region and bring it closer to the nozzle. The turbulence for the serrated nozzle decays much faster than that for the baseline downstream. It indicates that the serration-induced mixing increases the dissipation rate over that of the baseline. Looking at the turbulence distribution, the turbulence is generated differently at the tip and root. The turbulence at the root spreads more than that at the tip.

Since serration effects are close to the nozzle, radial profiles of velocity and turbulent fluctuations within $x/D = 1$ are further investigated. Figure 9(a) shows the velocity development near the nozzle. As noted previously, the shear layer from the tip develops at lower radial locations while that from the root is at higher radial locations. This difference is evident near the nozzle and gradually decreases as the jet develops downstream and spreads out radially. This increase the effective shear layer thickness. As for the turbulence development, the turbulent fluctuation profiles near the nozzle are shown in Fig. 9(b). The turbulence is initially intensified by serrations near the nozzle compared with the baseline. The peaks from the tip and root moves apart radially and gradually spreads out. The intensified peak decays fast as the energy is distributed more radially than the round jet.

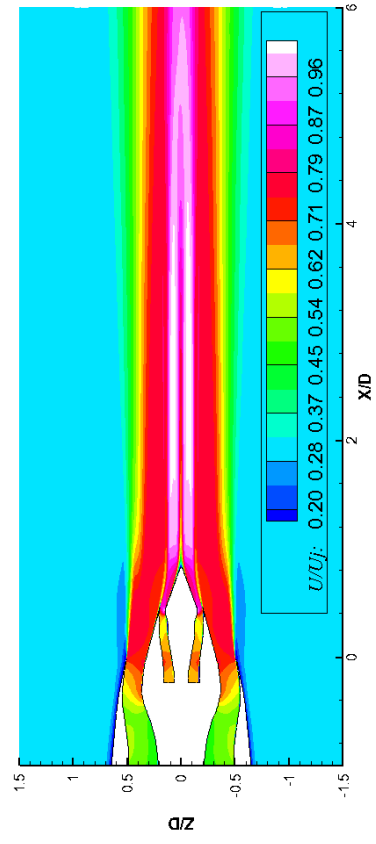
Figure 10(a) quantifies the mean radial locations of serration root and tip shear layer at different axial locations. This demonstrates the development of shear layer azimuthal variation. The root shear layer is brought inwards by the flight stream while the tip shear layer first contracts near the nozzle, then begins to spread after $x/D = 1$. The difference is taken between the root and tip and shown by the back line. The azimuthal difference first develops within $x/D = 0.5$ then plateaus until around $x/D = 1$. After that, turbulent mixing



(a) Axial velocity for the baseline jet

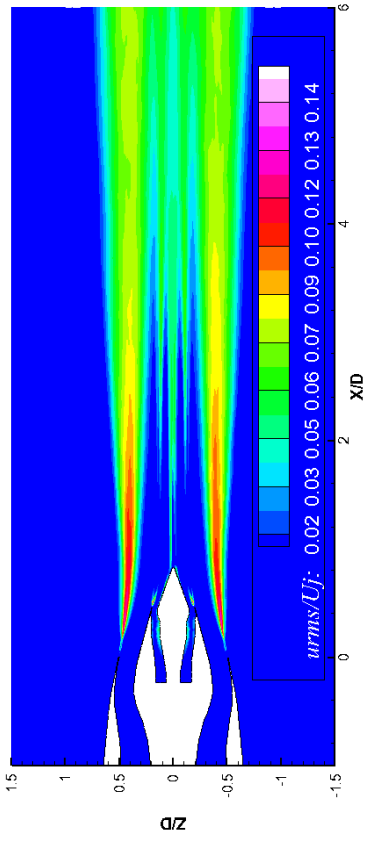


(b) Axial velocity at the serration tips

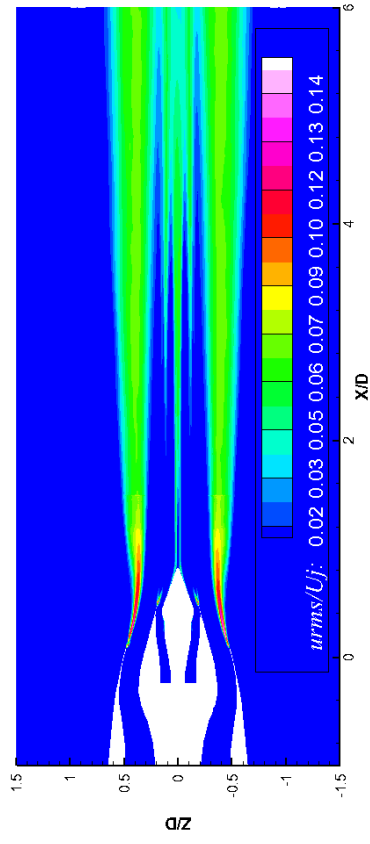


(c) Axial velocity at the serration roots

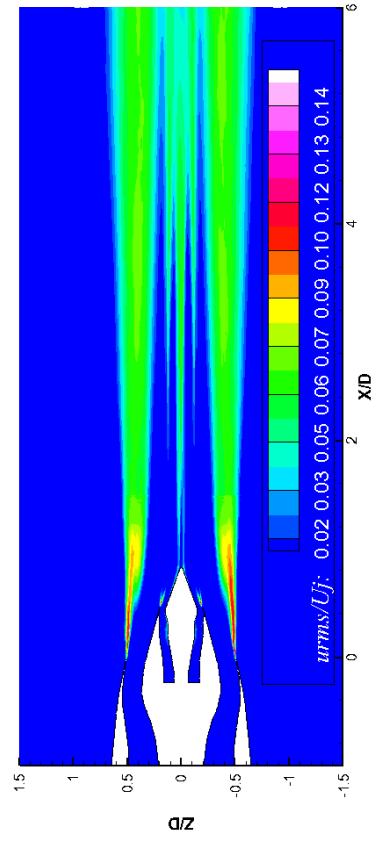
Figure 7: Time-averaged velocity field for the baseline and serrated nozzle jets



(a) Turbulent fluctuations for the baseline jet



(b) Turbulent fluctuations at the serration tips



(c) Turbulent fluctuations at the serration roots

Figure 8: Turbulent fluctuations for the baseline and serrated nozzle jets

becomes dominant, and the azimuthal difference decreases rapidly. Finally, the jet becomes azimuthally homogeneous after $x/D = 4$.

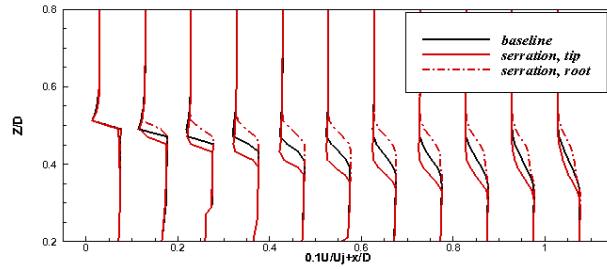
The development of turbulent fluctuations following the shear layer and centreline is shown in Fig. 10(b). The serration-induced streamwise vortices increase mixing near the nozzle so the turbulence in the shear layer decays sharply just downstream of the nozzle exit. The turbulence intensity is reduced to half of the initial level within two nozzle diameters downstream, while it takes around 12 diameters for the baseline round jets to reach this level. However, after $x/D = 2$ the serrated nozzle jet turbulence decreases gradually and finally the two jets decay to a similar level of turbulence far downstream at around $x/D = 15$. The centreline turbulence is also affected by the shear layer development. The first peak is caused by the interactions between outer bypass shear layer interactions with inner core jet shear layer and the second is caused by bypass shear layer merging at centreline. The first peak is intensified by serrations and the second peak is delayed and reduced by the rapid decay of serration shear layer turbulence.

4.2. Acoustics

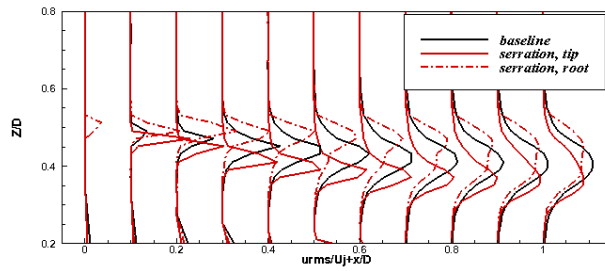
An overview of the near-field acoustics is shown in Fig. 5. The acoustic waves are emitted by the sound sources near the nozzle and interfere with each other. As the Goldstein analogy source [22, 23] is based on 4th order space-time correlations, they are used here to inform near-field jet noise sources. They are calculated by performing correlations between two Reynolds stress tensors, so expressed in a fourth order tensor:

$$R_{ijkl}(\vec{x}, \delta\vec{x}, \delta\tau) = \left\langle (\rho u'_i u'_j - \langle \rho u'_i u'_j \rangle)(\vec{x}, t) \cdot (\rho u'_k u'_l - \langle \rho u'_k u'_l \rangle)(\vec{x} + \delta\vec{x}, t + \tau) \right\rangle \quad (11)$$

The far-field sound can be obtained by integrating the correlations R_{ijkl} with the propagation Green functions in the source containing region [23]. Therefore, the space-time correlations are interpreted physically as the sound sources that

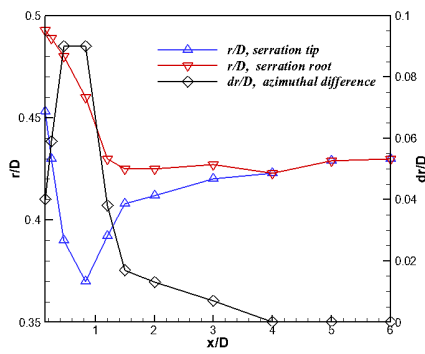


(a) Axial velocity

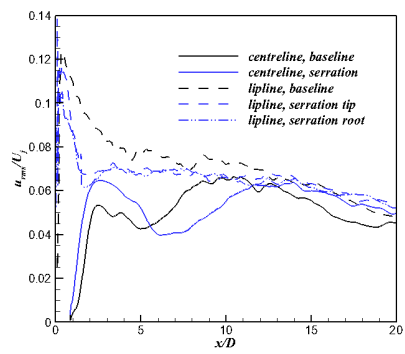


(b) Turbulent fluctuations

Figure 9: Radial profiles of axial velocity and turbulent fluctuations for the baseline and serrated nozzle jets within $x/D = 1$



(a) Shear layer azimuthal difference



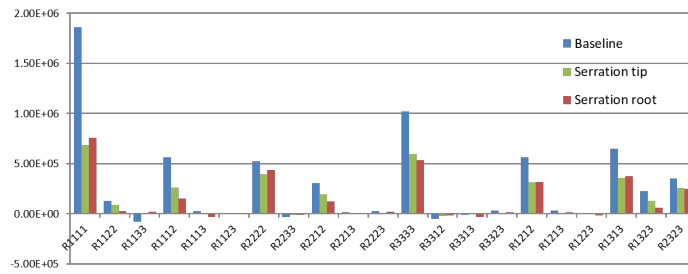
(b) Shear layer turbulent fluctuations

Figure 10: Shear layer development of azimuthal difference and turbulence fluctuations

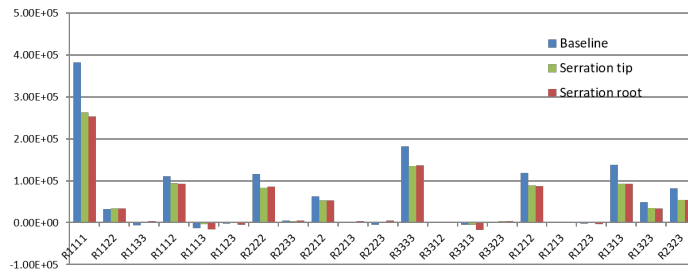
exhibit Gaussian distributions with turbulence temporal and spatial scales. The amplitude of the 4th order correlation $R_{ijkl}(\vec{x}, 0, 0)$ represents the sound source magnitude. As the sound source is mainly located inside shear layers, two representative axial location $x/D = 1$ and 10 are picked along the shear layers to show the sound source characteristics for both the round and serrated nozzle jets. $x/D = 1$ is near nozzle where turbulence is triggered by Kevin-Helmholtz instability and $x/D = 10$ is around potential core end where outer shear layers merge at the centre line. Over these two representative locations, there are some major components that prominently contribute to the sound sources. The dominant sound source component is R_{1111} (axial), while the secondary largest components are R_{2222} (radial) and R_{3333} (azimuthal). The remaining major components are shear stress correlations, R_{1212} , R_{1313} , R_{2323} , R_{1112} , R_{2212} and R_{1323} , which indicates the interactions between velocity components. In addition to what was observed by Karabasov et al. [23], R_{1112} , R_{2212} and R_{1323} are the new nonnegligible terms associated with axial-radial and axial-radial-azimuthal velocity interactions in these UHBPR nozzle jets.

In the near-nozzle region ($x/D = 1$), serrations can dramatically reduce the major sound source components near the nozzle and the reduction level at the serration tip and root is similar. The maximum reduction is seen on R_{1111} and then on R_{3333} and R_{1313} . This indicates that serrations have effects on reducing axial and azimuthal fluctuations. Moving downstream of the shear layer, the serration effect on source reduction becomes weaker at $x/D = 10$. Except on relatively large magnitude reduction on axial component R_{1111} , the reduction on other source components are benign. This indicates that the serration effects on sound source are more pronounced near the nozzle.

To understand this more comprehensively, the variation of the three major sound source components is plotted along the shear layers at different axial locations in Fig. 12. Figure 12(a) shows the absolute sound source amplitude up to axial distance of 15 D . The serrations make the sound source decay much faster compared to the baseline round jet. The source magnitude is rapidly reduced to a relatively low level before $x/D = 2$, while it takes 5-10 D for the



(a) $x/D = 1$



(b) $x/D = 10$

Figure 11: 4th order correlation amplitudes in the shear layer ($kg^2/(m^2s^4)$)

baseline jet to achieve this. At around $x/D = 15$, all the three major sound
 280 source components R_{1111} , R_{2222} and R_{3333} get to the same level as those of the
 baseline nozzle jet. This indicates that the serrations shorten the strong sound
 source containing region. In addition to this, the two components R_{2222} and
 R_{3333} develops differently from the baseline round jet near the nozzle. They
 are first intensified and exhibit a peak around $x/D = 1$, which might be related
 285 to the serration-introduced streamwise vortices. After this, they decay rapidly
 as R_{1111} does due to enhanced mixing. After normalization by the dominant
 component R_{1111} , the relative amplitudes of the other two source components,
 R_{2222} and R_{3333} are shown in Fig. 12(b). The relative amplitudes is at similar
 levels for the two jets, except that the baseline round jet shows slightly higher
 290 values around $x/D = 5$.

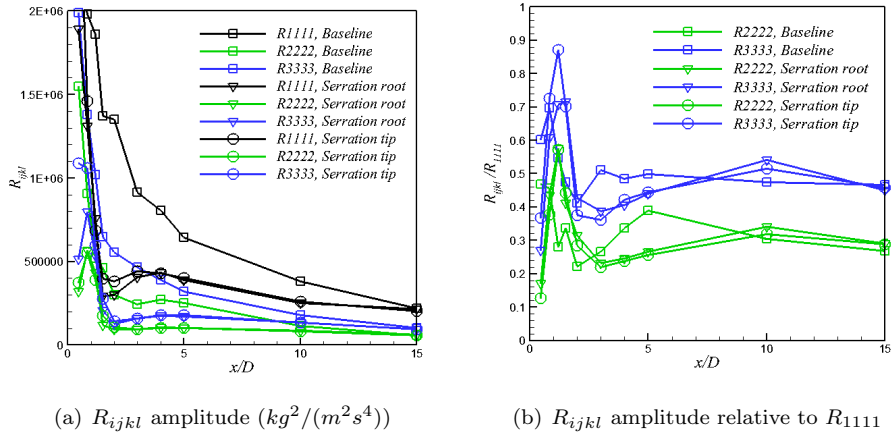
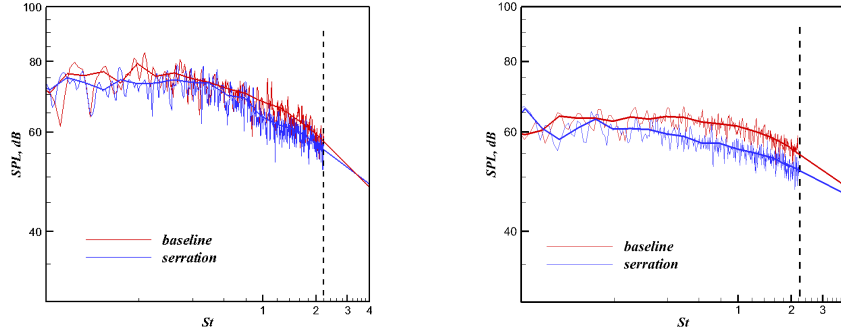


Figure 12: 4th order correlation amplitudes variation in the axial direction

Far-field sound spectra as shown in Fig. 13 have been calculated based on
 near-field FWH surface integrals. The 1/3 octave spectra is plotted with narrow
 spectra to better illustrate the trend. The Strouhal number ($St = \frac{fD_{bypass}}{U_{core}}$ that
 the current grid can resolve is up to around 2.4. The extrapolation has been
 295 made at the St limit by using the 1/3 octave spectra slope to show the spectra
 trend in high frequency range. The serrations tend to shift the acoustic energy
 from low to high frequencies. The spectra are about to cross at around $St=3$



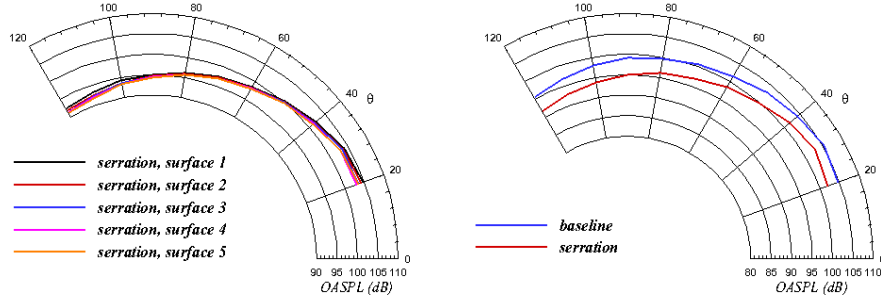
(a) sound spectra at 30° polar angle

(b) sound spectra at 120° polar angle

Figure 13: Far-field sound spectra prediction

for 30° degree while over $St=4$ for 120°. These are consistent with what was observed in the existing chevron design [2, 5].

300 As a series of surfaces with increasing radial position were placed in the near field, the sensitivity of far-field sound prediction to the surface locations is checked in Fig.14(a). It shows a convergent prediction of far-field sound from all surfaces, the maximum discrepancy among these surfaces are within 1.5dB. It has been shown that serrations can reduce noise over a range of low frequencies
 305 for this UHBPR jet. Although the trend of increased sound pressure level in high frequencies is demonstrated by extrapolating the spectra at the current resolved St limit, the high-frequency penalties are not directly evaluated in the overall sound pressure level (OASPL). Accordingly, OASPL is obtained by integrating the spectra from $St=0.06$ to 2.4, considering only low-frequency noise reduction.
 310 Figure 14(b) shows the comparison of OASPL between the baseline round and serration jets. The serrations reduce the overall farfield sound level by 2-4 dB in the low frequency range. When high frequency penalties are considered, the overall noise reduction might be reduced. This is to be confirmed in the future study by using a refined mesh to resolve larger frequency range.



(a) OASPL prediction on all FW-H surfaces (b) OASPL for the baseline and serration jets

Figure 14: Overall sound pressure level (OASPL) integrated over the frequency range ($St=0.06-2.4$)

315 5. Conclusions

High-resolution LES is performed for complex geometry UHBPR jets with and without serrations. Non-dissipative numerics are utilised employing a KEP scheme with 4th order smoothing, allowing modular hybrid structured-unstructured meshes to be used. A mixed non-linear SGS model is used in the LES region and hybridized with the SA RANS to model boundary layers on the nozzle. The shear layer from the serrated nozzle is inhomogeneous azimuthally, so a modular hybrid mesh is used to follow the serrated nozzle shear layer, facilitating mesh generation and also increasing mesh quality.

The results show that serration effects are evident near the nozzle for both mean flow velocity and turbulent fluctuations. The flow spreads rapidly from serration roots and contracts from the tips. This forms streamwise vortices and induces shear layer azimuthal variation. The azimuthal variation develops in the first $1D$ downstream then decays quickly when the mixing becomes dominant. The serrated nozzle jet finally returns to a round jet at $x = 4D$. The streamwise vortices thicken the shear layer and introduce small scale turbulence near the nozzle. Therefore, the turbulent fluctuations are intensified in the nozzle exit region and dissipated rapidly to half of the initial level by $x = 2D$ due to enhanced mixing. Turbulent fluctuations for the serrated nozzle jet remain

lower than the round jet until $x = 15D$. For the serrated nozzle, the extent of
335 the high turbulence region is reduced and moves upstream.

The near-field sound source is indicated by 4th order space-time correlations based on Goldstein acoustic analogy. The major source components are R_{1111} , R_{2222} , R_{3333} , R_{1212} , R_{1313} , R_{2323} , R_{1112} , R_{2212} and R_{1323} . Among them, R_{1111} dominates and is followed by R_{2222} and R_{3333} . R_{1112} , R_{2212} and R_{1323} is
340 new non-small axial-radial and axial-radial-azimuthal interaction components of sound sources in these UHBPR jets compared with the previous single stream round jets [23]. The serrations dramatically reduce the amplitude of major sound sources. As also reflected by the turbulence levels, the serrated nozzle sound sources decay rapidly near the nozzle and remain at a lower level than
345 the baseline from $x = 2D$ to $15D$. This makes sound sources more concentrated near the serrated nozzle exit and shortens the high-intensity source containing region.

Based on the near-field surface data, the convective FW-H formula is used to predict farfield sound for the UHPBR jet subject to a forward flight stream. LES
350 along with FW-H integration displays a convergent far-field sound prediction. It shows that the serrations reduce noise in the low frequencies. The OASPL in the far field has been reduced by 2-4 dB for the serrated nozzle jet when integrating low-frequency sound up to $St=2.4$. In the future, this LES data could be used to complement or replace data from experiments and aid the development of
355 noise reductions strategies in the aspects of cost and data richness.

Acknowledgement

The work is performed under the EU-funded project JERONIMO (ACP2-GA-2012-314692-JERONIMO) and the ARCHER computing time provided by the UK Turbulence Consortium under EPSRC grant EP/L000261/1. The fruit-
360 ful discussions with Dr. Peer Boehning from Rolls-Royce Deutschland are also greatly acknowledged.

References

- [1] M. J. Lighthill, On sound generated aerodynamically: I. general theory, Proc.R.Soc.Lond. A 211 (1952) 564587.
- 365 [2] S. Martens, Jet noise reduction technology development at GE aircraft engines, ICAS 2002 congress 842.
- [3] P. Jordan, T. Colonius, Wave packets and turbulent jet noise, Annu. Rev. Fluid Mech. 45 (2013) 173195.
- [4] M. B. Alkistar, A. Krothapalli, G. W. Bulter, The effect of streamwise
370 vortices on the aeroacoustics of a Mach 0.9 jet, J. Fluid Mech. 578 (2007) 139169.
- [5] K. B. M. Q. Zaman, J. E. Bridges, D. L. Huff, Evolution from tabs to chevron technology: a review, Int. J. Aeroacoustics 10 (2011) 685710.
- [6] C. E. Tinney, P. Jordan, The near pressure field of coaxial subsonic jets, J.
375 Fluid Mech. 611 (2008) 175–204.
- [7] V. G. Mengle, R. Elkoby, L. Brusniak, Reducing propulsion airframe aeroacoustic interactions with uniquely tailored chevrons: 1. isolated nozzle, AIAA paper 2006–2433.
- [8] V. G. Mengle, R. Elkoby, L. Brusniak, Reducing propulsion airframe aeroacoustic interactions with uniquely tailored chevrons: 2. installed nozzle,
380 AIAA paper 2007–2434.
- [9] V. G. Mengle, R. Stoker, L. Brusniak, R. Elkoby, Flapron modification effect on jet-flap interaction noise reduction for chevron nozzles, AIAA paper 2007–3666.
- 385 [10] M. L. Shur, P. R. Spalart, M. K. Strelets, A. K. Travin, Towards the prediction of noise from jet engines, Int. J. Heat and Fluid Flow 24 (2003) 551561.

- [11] Z.-N. Wang, I. Z. Naqavi, M. Mahak, P. Tucker, X. Yuan, P. Strange, Far field noise prediction for subsonic hot and cold jets using large-eddy simulation, ASME paper GT2014–27290. 390
- [12] Z.-N. Wang, I. Z. Naqavi, M. Mahak, P. G. Tucker, P. Boehning, Large-eddy simulation of the flight stream effects on single stream heated jets, AIAA paper 2017–0457.
- [13] H. Xia, P. G. Tucker, Numerical simulation of single-stream jets from a serrated nozzle, Flow Turbulence Combust. 88 (2012) 318. 395
- [14] J. Tyacke, I. Naqavi, Z.-N. Wang, P. G. Tucker, P. Boehning, Predictive LES for jet aeroacoustics: Current approach and industrial application, ASME. J. Turbomach. 139 (2017) 081003–081003–13. doi:doi:10.1115/1.4035662.
- [15] J. C. Tyacke, Z.-N. Wang, P. G. Tucker, LES-RANS of installed ultra-high bypass-ratio coaxial jet aeroacoustics with a finite span wing-flap geometry and flight stream - part 1: round nozzle, AIAA paper 2017–3854. 400
- [16] A. Jameson, Formulation of kinetic energy preserving conservative schemes for gas dynamics and direct numerical simulation of one-dimensional viscous compressible flow in a shock tube using entropy and kinetic energy preserving schemes, J Sci Comput 34 (2008) 188–208. 405
- [17] Z.-N. Wang, J. Tyacke, P. Tucker, Hybrid LES/RANS predictions of flows and acoustics from an ultra-highbypass-ratio serrated nozzle, Note on Numerical Fluid Mechanics and Multidisciplinary Design: Progress in Hybrid RANS-LES Modeling (2018) 1–12(in press). 410
- [18] P. Tucker, Differential equation-based wall distance computation for DES and RANS, Journal of Computational Physics 190 (1) (2003) 229–248. doi: [http://dx.doi.org/10.1016/S0021-9991\(03\)00272-9](http://dx.doi.org/10.1016/S0021-9991(03)00272-9).
- [19] P. R. Spalart, S. R. Allmaras, A one-equation turbulence model for aerodynamic flows, Recherche Aérospatiale 1 (1994) 5–21. 415

- [20] Y. Liu, P. G. Tucker, R. M. Kerr, Linear and nonlinear model large-eddy simulations of a plane jet, *Computers & Fluids* 37 (2008) 439449.
- [21] A. Najafi-Yazdi, G. A. Bres, L. Mongeau, An acoustic analogy formulation for moving sources in uniformly moving media, *Proc.R.Soc.Lond.* Adoi : 10.1098/rspa.2010.0172.
- [22] M. E. Goldstein, A generalized acoustic analogy, *J. Fluid Mech.* 488 (2003) 315333.
- [23] S. Karabasov, M. Afsar, T. Hynes, A. Dowling, W. McMullan, C. Pokora, G. Page, J. McGuirk, Jet noise: acoustic analogy informed by large eddy simulation, *AIAA journal* 48 (7) (2010) 1312.

Appendix: Methodology validation

The simulation methods used in this paper has been validated vastly in the previous research [11, 12, 13, 14, 17]. The typical results are summarized in 15. They includes far-field sound level predictions of five jets in comparison with experiment measurement. The nozzle covers round and serrated shape and the operating condition covers the hot and cold jets with and without flight stream. The discrepancy between the predicted and measured value is less than 2 dB. More details of the validation can be found in the published papers mentioned above.

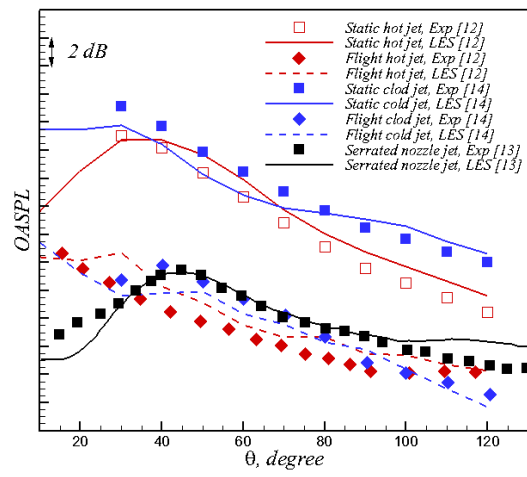


Figure 15: Summary of validated jet noise prediction